The Astrophysical Journal, 724:131–139, 2010 November 20 doi:10.1088/0004-637X/724/1/131

AMBIPOLAR DIFFUSION-MEDIATED THERMAL FRONTS IN THE NEUTRAL INTERSTELLAR MEDIUM

Jennifer M. Stone[1,2] and Ellen G. Zweibel[1,2,3]
[1] Department of Astronomy, University of Wisconsin–Madison, 475 North Charter Street, Madison, WI 53706, USA
[2] Center for Magnetic Self-Organization in Laboratory and Astrophysical Plasmas,
University of Wisconsin, 1150 University Avenue, Madison, WI, 53706, USA
[3] Department of Physics, University of Wisconsin–Madison, 1150 University Avenue, Madison, WI 53706, USA
Received 2010 June 23; accepted 2010 September 13; published 2010 October 28

ABSTRACT

In a thermally bistable medium, cold, dense gas is separated from warm, rarefied gas by thin phase transition layers, or fronts, in which heating, radiative cooling, thermal conduction, and convection of material are balanced. We calculate the steady-state structure of such fronts in the presence of magnetic fields, including the processes of ion–neutral drift and ion–neutral frictional heating. We find that ambipolar diffusion efficiently transports the magnetic field across the fronts, leading to a flat magnetic field strength profile. The thermal profiles of such fronts are not significantly different from those of unmagnetized fronts. The near uniformity of the magnetic field strength across a front is consistent with the flat field strength–gas density relation that is observed in diffuse interstellar gas.

Key words: diffusion – ISM: structure – magnetohydrodynamics (MHD) – methods: numerical

Online-only material: color figure

1. INTRODUCTION

The low- and intermediate-temperature parts of the interstellar medium (ISM) constitute a thermally bistable medium that results from the balance between radiative heating and cooling as well as heating by cosmic rays (Field et al. 1969) and photoelectric heating from polycyclic aromatic hydrocarbons (PAHs; Wolfire et al. 1995), the dominant heating source. The two stable phases are referred to as the cold neutral medium (CNM), having $T_{\rm CNM} \sim 10^{1-2}$ K, and the warm neutral medium (WNM), with $T_{\rm WNM} \sim 10^{3-4}$ K. The degree to which magnetic fields are frozen into this interstellar gas is parameterized by the magnetic Reynolds number, $Re_{\rm M}$, and the ambipolar Reynolds number, $Re_{\rm AD}$ (Zweibel & Brandenberg 1997). The magnetic Reynolds number is given by the ratio of the Ohmic diffusion time to the dynamical time, and for ISM parameters it is of order 10^{15}–10^{21}. The ambipolar Reynolds number, given by the ratio of the ion–neutral drift time to the dynamical time, is many orders of magnitude smaller and may approach unity in dense molecular gas. Based on these estimates, one would expect that magnetic fields should be well coupled to both the ionized part of the gas and to the neutrals for all but the most dense or low column density clouds.

Under ideal magnetohydrodynamic (MHD) conditions, such as those indicated above, one might expect a strong correlation between magnetic field strength and density. If the relationship is expressed as $B \propto \rho^{\chi}$ and we ignore diffusion, for flows directed transverse to the field we have $\chi = 1$, whereas for field aligned flows $\chi = 0$. The median magnetic field strength in the CNM has been measured at $B \sim 6\,\mu$G (Heiles & Troland 2005). If the field was frozen in, we might expect to detect much smaller field strengths in warmer, lower density gas, but instead it is found that the field strength in other ISM components is similar to that of the CNM. This was demonstrated by measurements of the Zeeman effect over the density range $0.1\,{\rm cm}^{-3} < n < 100\,{\rm cm}^{-3}$ that yielded a flat magnetic field strength–gas density (B–ρ) relation (Troland & Heiles 1986). The most obvious explanation for this relation is that motions are aligned with the magnetic field. However, this has been argued against in two ways. First, in order for a magnetic field to collimate a flow in this manner, it must dominate the turbulent energy density, but the field strength is less than or equal to equipartition (Heitsch et al. 2004). Second, the accumulation length for the formation of giant molecular clouds is of order a kiloparsec and may be too large a scale over which to expect coherent flows (Mestel 1985). Thus, the flat B–ρ relation may be indicative of magnetic diffusion.

Among the mechanisms that have been proposed to account for the flat B–ρ relation in the diffuse ISM are turbulent ambipolar diffusion (Zweibel 2002; Heitsch et al. 2004), decorrelation due to MHD waves (Passot & Vázquez-Semadeni 2003), and turbulent magnetic reconnection (e.g., Santos-Lima et al. 2010). These dynamical studies argued that ambipolar diffusion alone was not sufficiently fast to transport magnetic flux over the large scales under consideration and so invoked turbulence to enhance transport. However, a one-dimensional two-fluid dynamical study of the thermal instability as a formation mechanism for diffuse clouds showed ambipolar diffusion to efficiently transport magnetic field such that the observed B–ρ relation could be reproduced (Inoue et al. 2007). The work presented here complements those findings but is also a significant departure from that and the other cited examples as we shall consider the actual transitions from one phase to another. Our approach is advantageous in that we control the diffusive processes and are not hampered by numerical diffusion. The hydrodynamic structure of CNM/WNM transitions has already been presented (Inoue et al. 2006, hereafter IIK06), but the effects of a magnetic field have not previously been studied. In the case of a magnetic field orthogonal to a transition layer, the field has no effect on the structure as it does not exert any force or modify thermal conduction in the direction of the temperature gradient, although it has a large effect on stability (Stone & Zweibel 2009). In this work, we consider the case of a magnetic field tangential to a transition layer in a simple one-dimensional geometry and include ion–neutral drift as the magnetic diffusion mechanism.

Our paper is organized as follows. In Section 2, we present our numerical method for calculating the structure of a phase transition layer for a given initial density and magnetic field strength.

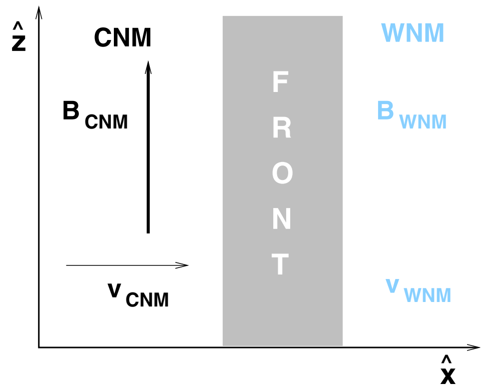

Figure 1. Geometry of front and magnetic field. We seek a front solution connecting the CNM with the WNM for the case of a uniform magnetic field tangential to the front, $\boldsymbol{B}_{\rm CNM} = B(x)\hat{z}$. The bulk velocity flow is in the x-direction. The WNM quantities to the right of the front are to be solved for.

(A color version of this figure is available in the online journal.)

In Section 3, we discuss the effect of ambipolar drift heating on the two-phase structure of the neutral ISM. In Section 4, we show a selection of our ambipolar diffusion-mediated front solutions and include a brief discussion of the flux-freezing approximation. In Section 5, we discuss the physical significance of our results, and in Section 6, we summarize our findings.

2. METHOD

We consider the scenario of a phase transition layer, or front, separating two uniform media of different densities and temperatures in a simple one-dimensional geometry with x as the direction of variation. A uniform magnetic field is tangential to the front such that $\boldsymbol{B} = B(x)\hat{z}$. The geometry is illustrated in Figure 1. We assume a steady-state and ionization equilibrium and work in the reference frame of the front. These assumptions shall be justified in Section 5. In order to calculate the physical structure of a front we consider six variables: pressure (p), density (ρ), bulk velocity (v), plasma velocity (v_p), magnetic field strength (B), and temperature (T) that are described by the following five equations, namely, the equation of state

$$p = \frac{R\rho T}{\mu}, \tag{1}$$

the continuity equation

$$\frac{\partial \rho}{\partial t} + \frac{\partial}{\partial x}\rho v = 0, \tag{2}$$

the momentum equation

$$\frac{\partial \rho v}{\partial t} + \frac{\partial}{\partial x}\left(\rho v^2 + p + \frac{B^2}{8\pi}\right) = 0, \tag{3}$$

the induction equation

$$\frac{\partial B}{\partial t} = -\frac{\partial}{\partial x}(v_p B), \tag{4}$$

and the energy equation

$$\frac{\gamma}{\gamma - 1}\frac{R}{\mu}\rho\frac{dT}{dt} - \frac{dp}{dt} = \frac{\partial}{\partial x}\kappa\frac{\partial T}{\partial x} - \rho\mathcal{L}, \tag{5}$$

where γ is the adiabatic index, R is the molar gas constant, μ is the mean molecular weight, κ is the thermal conductivity, $\rho\mathcal{L}$ is the cooling function (which includes ambipolar drift heating), and $d/dt \equiv \partial/\partial t + v\,\partial/\partial x$. In the approximation that the plasma and neutral fluids are well coupled, and the neutral density dominates, the plasma velocity may be written as the sum of the drift velocity, $v_D = v_i - v_n$, and center of mass velocity, $v \approx v_n$, such that $v_p \approx v + v_D$, where the drift velocity is given by Shu (1983):

$$\boldsymbol{v}_D = \frac{\boldsymbol{J} \times \boldsymbol{B}}{c\rho_i\rho_n\gamma_{\rm AD}}, \tag{6}$$

with the drag coefficient for collisions between ions and neutrals given by $\gamma_{\rm AD} = \langle\sigma v\rangle_{\rm in}/(m_i + m_n)$ cm^3 s^{-1} g^{-1}, where $\langle\sigma v\rangle_{\rm in} = 2 \times 10^{-9}$ cm^3 s^{-1} (Draine et al. 1983).

Assuming a steady-state (and having already dropped the $\hat{y}$ and $\hat{z}$ dimensions), integrating Equations (2), (3), and (5) with respect to x yields the following conservation laws:

$$j \equiv \rho v, \tag{7}$$

$$M_B \equiv \rho v^2 + p + \frac{B^2}{8\pi}, \tag{8}$$

$$\frac{\gamma}{\gamma - 1}\frac{R}{\mu}j\frac{dT}{dx} - v\frac{dp}{dx} = \frac{\partial}{\partial x}\kappa\frac{\partial T}{\partial x} - \rho\mathcal{L}, \tag{9}$$

where j is the mass flux and M_B is the total energy density. To solve Equation (9), we require expressions describing the evolution of the flow speed and magnetic field strength, including the process of ambipolar diffusion. An equation for the flow speed is obtained by taking the derivative of the total energy density, Equation (8), to obtain

$$\frac{dv}{dx} = \frac{\left(\mu v^2 B\frac{dB}{dx} + 4\pi R j v\frac{dT}{dx}\right)}{4\pi j(RT - \mu v^2)}. \tag{10}$$

An equation describing the magnetic field strength is derived by substituting $\boldsymbol{B} = B(x)\hat{z}$ into Faraday's law in one dimension and using Equation (4) to yield

$$\frac{\partial B_z}{\partial t} = -c\frac{\partial E_y}{\partial x} \Rightarrow cE_y = -(v_p \times B)_y = v_{px}B_z = \text{constant}. \tag{11}$$

Substituting the plasma velocity, with the drift velocity given by Equation (6), into Equation (11) we obtain

$$vB - \frac{B^2}{4\pi\rho_i\rho_n\gamma_{\rm AD}}\frac{dB}{dx} = cE. \tag{12}$$

This is a first-order ordinary differential equation (ODE) with one parameter, cE. Mathematically, cE can take any value since it is a constant of integration. However, we will argue at the end of this section that physical considerations of the magnetic field strength and ambipolar heating across a front serve to greatly reduce the cE parameter space.

Equations (9), (10), and (12), and the definition $z \equiv dT/dx$ yield a system of four ODEs for T, B, and v that apply for any functional form of conductivity and cooling function. In the gas states studied here, conductivity is dominated by neutral atoms such that $\kappa = 2.5 \times 10^3\, T^{1/2}$ erg s^{-1} K^{-1} cm^{-1} (Parker 1953). The cooling function is written in full as

$$\rho\mathcal{L} = n[n\Lambda - (\Gamma_{\rm PAH} + \Gamma_{\rm AD})]. \tag{13}$$

We take the simple functional forms used by IIK06 for Lyα and [C II] radiative cooling such that

$$\Lambda = 7.3 \times 10^{-21} \exp\left(\frac{-118,400\,\mathrm{K}}{\mathrm{T} + 1500\,\mathrm{K}}\right) + 7.9 \times 10^{-27} \exp\left(\frac{-92\ \mathrm{K}}{\mathrm{T}}\right) \mathrm{erg\ \ s^{-1}\,cm^{-3}}, \quad (14)$$

and for photoelectric heating

$$\Gamma_{\mathrm{PAH}} = 2 \times 10^{-26}\,\mathrm{erg \quad s^{-1}}. \quad (15)$$

Heating by ion–neutral friction is represented by Γ_{AD}:

$$n\Gamma_{\mathrm{AD}} = \rho_i \rho_n \gamma_{\mathrm{AD}} v_D^2 = \frac{1}{\rho_i \rho_n \gamma_{\mathrm{AD}}} \left(\frac{B}{4\pi} \frac{dB}{dx}\right)^2 \mathrm{erg\ \ s^{-1}\,cm^{-3}} \quad (16)$$

(Scalo 1977; Padoan et al. 2000), where the density of neutrals is given by $\rho_n = \mu_n m_H n$ and the density of ions by $\rho_i = \mu_i m_p n_e$. We compute the ionization fraction using

$$\frac{n_e}{n_{\mathrm{H}}} = \left(1.19 \times 10^{-4} - 1.36 \times 10^{-8} \frac{T^{0.845}}{n_{\mathrm{H}}}\right) + \left(1.42 \times 10^{-8} + 2.72 \times 10^{-8} \frac{T^{0.845}}{n_{\mathrm{H}}} + 1.85 \times 10^{-16} \frac{T^{1.69}}{n_{\mathrm{H}}^2}\right)^{1/2} \quad (17)$$

(Ferrière et al. 1988).

In solving this system, we choose initial values for the density and magnetic field strength and impose the following boundary conditions:

$$T(x = x_1) = T_1, \quad T(x = x_2) = T_2, \quad (18)$$

$$\left.\frac{dT}{dx}\right|_{x_1, x_2} = 0, \quad (19)$$

where x_1 and x_2 represent the left- and right-hand boundaries, respectively, and T_1 and T_2 satisfy thermal equilibrium at these boundaries. T_1 is found by solving Equation (13) for the chosen initial value of the density at x_1, and T_2 is the temperature obtained by integrating as far as x_2, where the size of the domain is chosen such that T_2 will also satisfy thermal equilibrium. For our third and fourth conditions, given by Equation (19), we impose zero temperature gradient at both boundaries. Finally, we set the value of the initial magnetic field strength gradient, $|dB/dx|_{x_1}$, as this controls the amount of ambipolar heating in a given front model. As we will show in Section 4, the choice of the initial field strength gradient affects the structure of the front. Given that we set five boundary values but have a system of only four ODEs, we thus set up an eigenvalue problem in which the mass flux, j, is the parameter to be adjusted to find a self-consistent solution.

The numerical method we employ is that of shooting, in which the integration is performed with an initial guess for j, the resulting boundary values compared to the desired conditions, and j adjusted accordingly so that the integration can be repeated as necessary until the right-hand boundary conditions are satisfied to within some chosen tolerance. We find that the degree to which thermal equilibrium is satisfied at the right-hand boundary depends on the size of the domain, which should be adjusted to achieve optimum results. For cases in which ambipolar drift heating does not dominate, it is possible to satisfy thermal equilibrium to better than one part in 10^5. We use a fifth-order adaptive Runge–Kutta scheme (Press et al. 1992) and adjust the eigenvalue according to the secant method. When appropriate bounds are chosen, our method converges to a solution quickly, requiring of order 10 iterations. Note that we always integrate from the cold medium to the warmer one.

We close this section with a brief discussion of the initial magnetic field strength gradient boundary condition and the parameter cE. In setting up our initial conditions, instead of choosing the value of cE directly we instead set the initial value of the magnetic field strength gradient, $|dB/dx|_{x_1}$. This implies the value of cE, which is kept constant across the domain, as we may evaluate it by substituting our initial conditions into Equation (12). Note that the value of cE will change with each iteration of the shooting method because it depends on the bulk velocity, which is adjusted according to the secant method. For all density and magnetic field strength initial conditions, there is some minimum value of cE below which the magnetic field strength gradient is positive throughout the domain. The outcome for choosing an initial field gradient that yields a value of cE below this minimum would be a larger magnetic field strength in the warm medium than in the colder one. However, if one imagines an evaporating cool cloud with the assumption of frozen-in magnetic field lines, this does not seem like a physically reasonable scenario as the field lines will become further apart as the cloud expands. Furthermore, if the value of cE is too large, ambipolar drift heating may dominate over photoelectric heating making it increasingly difficult to satisfy thermal equilibrium at the far boundary, implying that a front can no longer exist. We demonstrate quantitatively the effects of $|dB/dx|_{x_1}$, and hence cE, in Section 4, but do not refer to cE explicitly in the rest of the paper.

3. EFFECTS OF AMBIPOLAR DRIFT HEATING ON TWO-PHASE STRUCTURE

The two neutral phases of the ISM are enabled by the balance of radiative cooling and heating by, in this work, photoelectric heating and ion–neutral friction. We present the equilibrium state of the cooling function, $\rho\mathcal{L}\ (n, T) = 0$, in Figure 2, with $\rho\mathcal{L}$ given by Equation (13). The solid line shows the case in which there is no ambipolar drift heating, for which IIK06 report that a two-phase structure is possible for $10^{2.8}\ \mathrm{K\,cm^{-3}} < p/k_B < 10^{4.1}\ \mathrm{K\,cm^{-3}}$ (where k_B is the Boltzmann constant). The other lines illustrate the effects of increasing the ambipolar drift heating rate at a fixed magnetic field strength of 3 μG. Although we have already shown Γ_{AD} to be a function of the density and field strength, for the purposes of this plot we have set it to be a constant fraction of the photoelectric heating rate, Γ_{PAH}. Increasing the total heating rate serves to increase the pressure at which two phases can coexist: the minimum pressure at which the cold phase can exist and the maximum pressure at which the warmer phase can exist both increase. In fact, the pressure range over which two phases can exist becomes larger as the total heating is increased. For example, for the $\Gamma_{\mathrm{AD}}/\Gamma_{\mathrm{PAH}} = 0.50$ case plotted in Figure 2, two-phase structure is possible for $10^{3.0}\ \mathrm{K\,cm^{-3}} < p/k_B < 10^{4.3}\ \mathrm{K\,cm^{-3}}$, and for the $\Gamma_{\mathrm{AD}}/\Gamma_{\mathrm{PAH}} = 1.00$ case the pressure range is $10^{3.1}\ \mathrm{K\,cm^{-3}} < p/k_B < 10^{4.4}\ \mathrm{K\,cm^{-3}}$. We can understand the shift toward lower densities as follows: increasing the heating

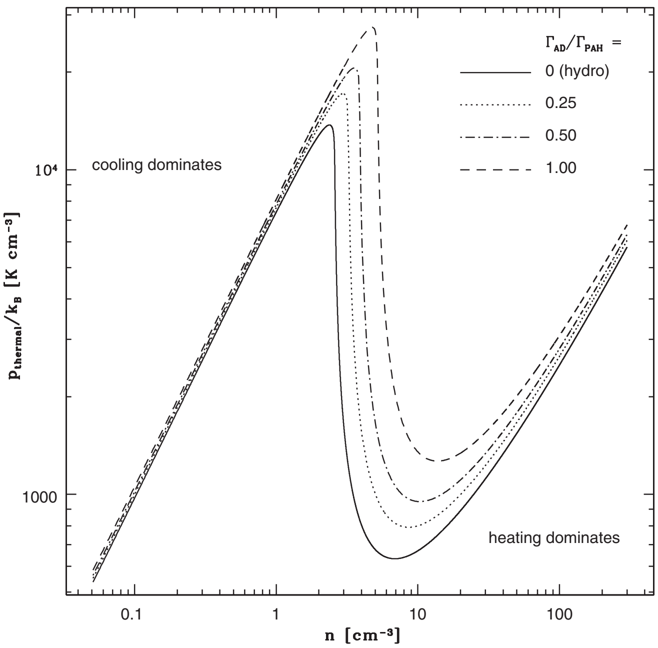

Figure 2. Thermal equilibrium state of the cooling function, $\rho\mathcal{L}\,(n,T) = 0$, in the thermal pressure–number density plane. The solid line shows the hydrodynamic case in which there is no ambipolar drift heating. The other curves show the effect of increasing the ambipolar drift heating rate at a fixed magnetic field strength of 3 μG. In the area above the curves $\rho\mathcal{L} > 0$ so cooling dominates, while below the curves $\rho\mathcal{L} < 0$ so heating dominates. Increasing the ambipolar drift heating rate increases the pressure at which two phases can coexist. Note that the ambipolar drift heating rate is actually a function of density and magnetic field strength, as given by Equation (16), but for the purposes of this plot we set it to be some constant fraction of the photoelectric heating rate.

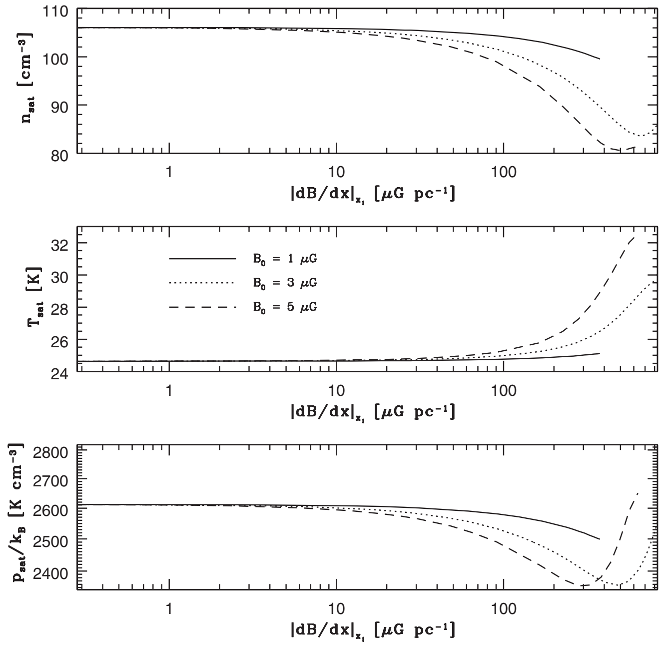

Figure 3. Saturation number density, temperature, and pressure (where $p_{sat}/k_B = n_{sat}T_{sat}$) as a function of the initial magnetic field strength gradient for initial field strengths of 1, 3, and 5 μG. The range of $|dB/dx|_{x_1}$ has been chosen to show the inflection point of the saturation pressure. The 1 μG curve has not been extended further because when $|dB/dx|_{x_1}$ is too large such a front cannot connect to a thermal equilibrium phase before the magnetic field strength becomes negative. The 3 and 5 μG curves can be extended to larger saturation pressures than shown here, until their magnetic profiles also become negative.

increases the temperature, so it must decrease the density. The upshift of the equilibrium to higher pressures also reflects the increased heating.

4. FRONT SOLUTIONS

The characteristics of a front are determined by its thermal pressure. There exists a "saturation pressure" at which heating and cooling are balanced within a front (Zel'dovich & Pikel'ner 1969; Penston & Brown 1970). If Λ and Γ can be written as functions of pressure and temperature (where Γ is the total heating rate), this pressure may be calculated by solving the integral (Inoue et al. 2006)

$$\int_{T_1}^{T_2} \kappa\rho\mathcal{L}\mathrm{dT} = \int_{T_1}^{T_2} \kappa\mathrm{n}(\mathrm{n}\Lambda - \Gamma)\mathrm{dT} = 0 \qquad (20)$$

and substituting for n using the equation of state, Equation (1). For the hydrodynamic case ($\Gamma_{AD} = 0$), IIK06 obtain $p_{sat}/k_B = 2612$ K cm^{-3}, which, by solving Equation (13), implies an initial density of $n = 106.08$ cm^{-3} and hence an initial temperature of $T = 24.63$ K. If the thermal pressure exceeds this value of p_{sat}, a fluid element passing through the front experiences net cooling, so we have a condensation front. If instead the thermal pressure is less than the saturation value a fluid element experiences net heating, so we have an evaporation front.

In this section, we demonstrate the effect of ambipolar diffusion on the saturation pressure and present our ambipolar diffusion-mediated front solutions. We also argue that the flux-freezing approximation is not accurate for steady-state thermal fronts.

4.1. *Effects of Ambipolar Drift Heating on Saturation Pressure*

The saturation pressure is altered in the presence of a magnetic field due to ambipolar drift heating. The integral given by Equation (20) cannot be solved analytically when Γ_{AD} is nonzero, so instead we use our shooting method, as discussed in Section 2, to find the initial density that yields a static solution as a function of the initial magnetic field strength gradient. The results for initial magnetic field strengths of 1, 3, and 5 μG are shown in Figure 3. Note that the field gradients are actually negative, as we anticipate the magnetic field strength to decrease with increasing temperature, and we refer to the absolute magnitude of the quantity, which we give in units of μG pc^{-1}.

As $|dB/dx|_{x_1}$ is increased, the saturation density and pressure for all magnetic field strengths initially decrease until a sufficiently large value of $|dB/dx|_{x_1}$ is reached, after which the density and pressure both increase. Therefore, it is possible to have two different fronts at the same saturation pressure. This non-monotonic behavior may be understood by solving Equation (20) for the saturation pressure using the equation of state, Equation (1), to obtain

$$\frac{p_{sat}}{k_B} = \frac{\Gamma\int_{T_1}^{T_2}\frac{\kappa}{T}dT}{\int_{T_1}^{T_2}\frac{\kappa\Lambda}{T^2}dT}. \qquad (21)$$

This shows that increasing the total heating rate, Γ, tends to increase the saturation pressure. But increased heating also tends to drive up the temperature, which for CNM temperatures greatly increases the cooling rate, Λ, and according to Equation (21) this decreases the saturation pressure. For example, Figure 3 shows that if $B_0 = 5\,\mu$G and $|dB/dx|_{x_1} =$

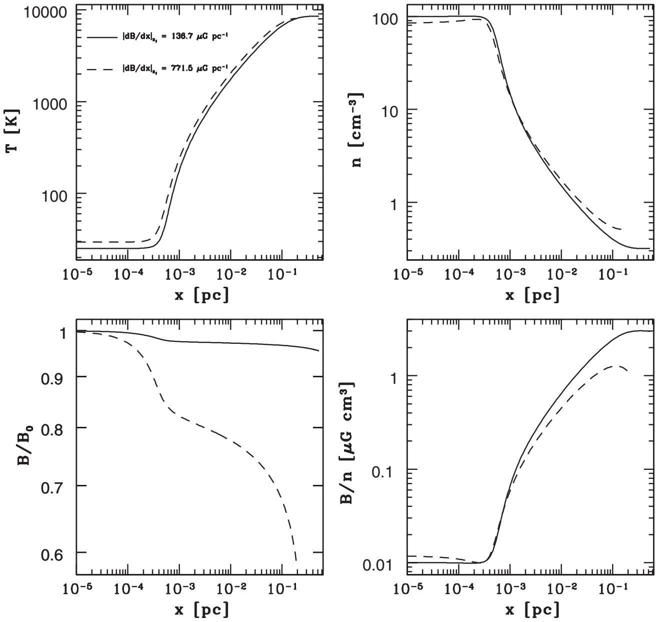

Figure 4. Two static fronts with $p_{\rm thermal}/k_B = 2500$ K cm^{-3} and an initial magnetic field strength of 3 μG, but different initial magnetic field strength gradients. Only the phase transition is shown, so the reader may find it helpful to picture the cold phase occupying the region $x < 0$, and the warmer medium filling the region beyond the end of the transition. The dashed line shows the front subject to a higher ambipolar diffusion heating rate, which connects a cold medium, with $n_{\rm CNM} = 84.66$ cm^{-3} and $T_{\rm CNM} = 29.53$ K, with a warmer medium with $n_{\rm WNM} = 0.52$ cm^{-3} and $T_{\rm WNM} = 8063$ K. The front with the lower ambipolar drift heating rate connects a cold phase having $n_{\rm CNM} = 95.51$ cm^{-3} and $T_{\rm CNM} = 25.12$ K with a warm phase having $n_{\rm WNM} = 0.32$ cm^{-3} and $T_{\rm WNM} = 8533$ K. The top panels show the temperature and density profiles, and the lower panels show the magnetic field strength profiles and the ratio of the field strength to the density for both models.

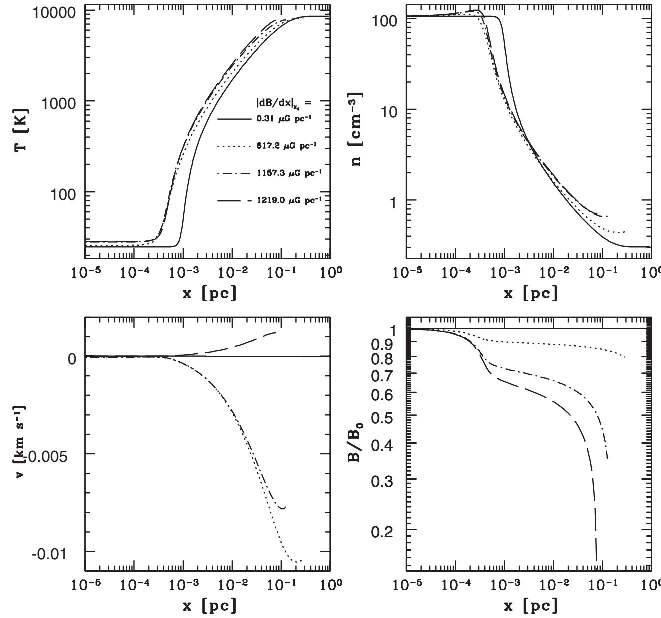

Figure 5. Profiles of fronts having an initial density of $n = 106.08$ cm^{-3} and an initial magnetic field strength of $B_0 = 3\,\mu$G for various initial magnetic field strength gradients. The top panels show the temperature and density profiles, and the lower panels show the bulk velocity and magnetic field strength profiles of the fronts. The different line styles represent different values of $|dB/dx|_{x_1}$ (note that these same line styles are used in Figures 6 and 7).

300 μG pc^{-1}, the CNM temperature is increased from 24 to 28 K. According to Equation (14), this results in a greater than 70% increase in the cooling rate, Λ. Such a large increase in cooling requires a lower density and a lower saturation pressure for equilibrium to be maintained. This effect dominates as long as the heating and cooling rates, Γ and Λ, are not too large and is the reason for the dip in the saturation pressure seen in Figure 3. An inflection point is not observed in the saturation pressure in the 1 μG case, the reason being that at higher values of $|dB/dx|_{x_1}$ (and hence larger ambipolar heating rates) the magnetic field profile is so steep that a thermal equilibrium phase cannot be reached before the magnetic field strength becomes negative. In such instances, the temperature on the cold side is still well within the range of CNM values, so it is not the medium being overheated that prohibits physical front solutions.

We present example saturation fronts having a thermal pressure of $p_{\rm th}/k_B = 2500$ K cm^{-3} and an initial field strength of 3 μG, but with different initial values of $|dB/dx|_{x_1}$, in Figure 4. Note that the values of $|dB/dx|_{x_1}$ given represent the largest gradients at any point throughout the front. The magnetic field strength gradients of all the fronts we present quickly relax to become much smaller than the initial values that we impose. The front having the larger value of $|dB/dx|_{x_1}$ has a higher ambipolar drift heating rate and connects a lower density, higher temperature CNM with a higher density, cooler WNM than the static front with the lower heating rate. The front with the lower ambipolar drift heating rate is the most diffusive, which is illustrated by its flatter magnetic field strength profile. This is also indicated by the ratio of the field strength to the number density, which shows a larger variation across the domain than the same quantity for the static front with the higher heating rate.

4.2. *Ambipolar Diffusion-mediated Front Solutions*

As stated at the beginning of Section 4, in the hydrodynamic case a static front has a thermal pressure of $p_{\rm sat}/k_B = 2612$ K cm^{-3}, which corresponds to an initial density and temperature of $n = 106.08$ cm^{-3} and $T = 24.63$ K, respectively. To demonstrate the effects of ambipolar diffusion, we present several front models having this same initial density and an initial magnetic field strength of 3 μG in Figure 5. The initial temperature changes according to the ambipolar drift heating rate, so it is not the same as in the hydrodynamic case. The different models correspond to various initial magnetic field strength gradients, $|dB/dx|_{x_1}$, where a larger gradient corresponds to increased heating. The properties of the phases connected by these fronts are listed in Table 1.

The overall shapes of the temperature profiles, shown in the top left panel of Figure 5, are fairly similar with the main differences being the temperature gradients on small scales and the final temperatures of the warm phases becoming lower as $|dB/dx|_{x_1}$ is increased. The main effect of increasing $|dB/dx|_{x_1}$ is that the size of the integration domain required to reach thermal equilibrium at the right-hand boundary becomes smaller due to the increased ambipolar drift heating. In fact, the lowest $|dB/dx|_{x_1}$ profile shown here is very similar to the hydrodynamic solution of IIK06. The top right panel of Figure 5 shows that the density varies by more than 2 orders of magnitude across the front for all heating rates. As $|dB/dx|_{x_1}$ is increased the density of the warm phase at the far boundary increases and hence the temperature decreases.

For insight into the actual nature of fronts, one may begin by looking at the bulk velocity profiles, shown in the bottom left panel of Figure 5. The effect of the initial magnetic field strength gradient on the velocity profile of a front is not

Table 1
Properties of Cold and Warm Phases Connected by Fronts[a] Having an Initial Density of $n_{\mathrm{CNM}} = 106.08\ \mathrm{cm}^{-3}$ and an Initial Magnetic Field Strength of $B_{\mathrm{CNM}} = 3\ \mu\mathrm{G}$

$\lvert dB/dx\rvert_{x_1}$ (μG pc^{-1})	Front Type	T_{CNM} (K)	n_{WNM} (cm^{-3})	T_{WNM} (K)	B_{WNM} (μG)	Thickness (pc)
0.31	Static	24.63	0.31	8580	3.000	0.94
617.2	Condensation	25.65	0.45	8210	2.386	0.28
1157.3	Condensation	27.97	0.67	7818	1.053	0.12
1219.0	Evaporation	28.30	0.72	7743	0.037	0.08

Note. [a] The profiles of the connecting fronts are presented in Figure 5.

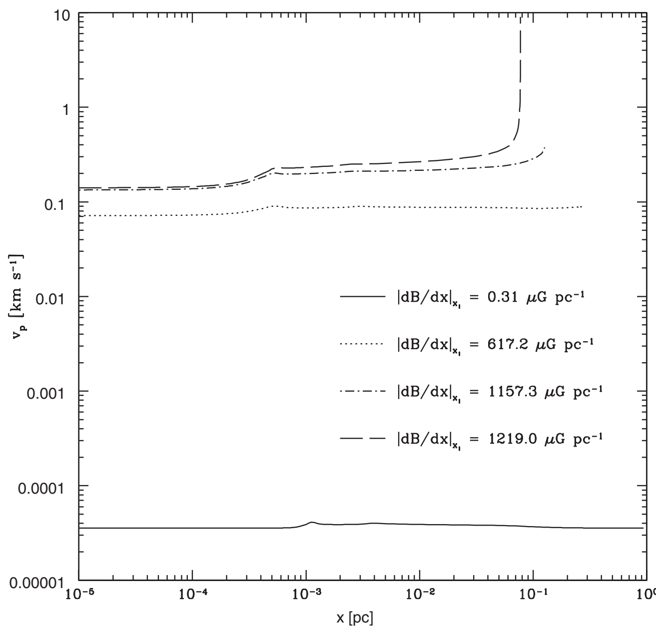

Figure 6. Plasma velocity ($v_p \approx v + v_D$) profiles of fronts having an initial density of $n = 106.08\ \mathrm{cm}^{-3}$ and an initial magnetic field strength of $B_0 = 3\ \mu$G for various initial magnetic field strength gradients.

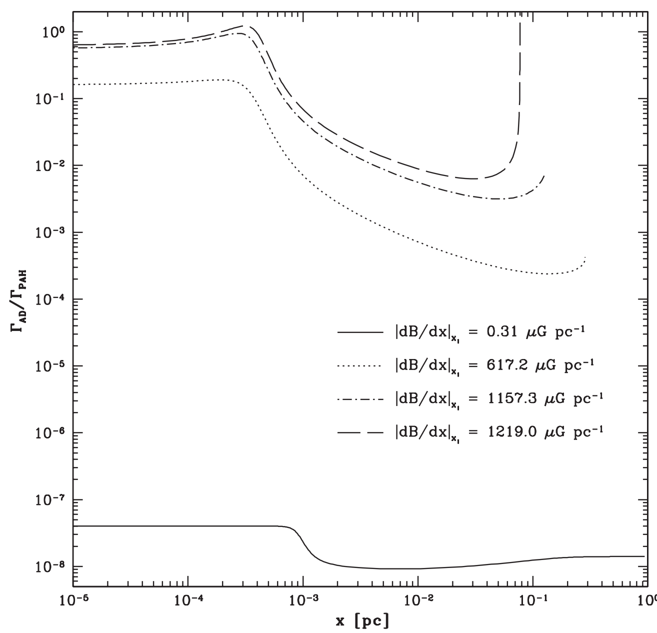

Figure 7. Ambipolar drift heating rates normalized by photoelectric heating rate across fronts having an initial density of $n = 106.08\ \mathrm{cm}^{-3}$ and an initial magnetic field strength of $B_0 = 3\ \mu$G for various initial field strength gradients.

straightforward. For the lowest initial $|dB/dx|_{x_1}$ case shown, the velocity profile is flat and close to zero, as should be the case for a static front. As $|dB/dx|_{x_1}$ is increased the velocity at first becomes larger and negative. This is because the saturation pressure is altered from the original hydrodynamic value of $p_{\mathrm{sat}}/k_B = 2612\ \mathrm{K\ cm}^{-3}$, as we discussed in Section 4.1. The models shown here with negative velocity profiles are actually condensation fronts. However, as $|dB/dx|_{x_1}$ is further increased there comes a point when the velocity no longer becomes increasingly negative and instead begins to increase. Eventually, the front transitions from being a condensation front to an evaporation front, which is illustrated by the positive velocity profile of the largest $|dB/dx|_{x_1}$ model shown in Figure 5. This is expected because of the non-monotonic behavior of the saturation pressure as the ambipolar heating rate is increased (see Figure 3).

The magnetic field strength profile of the lowest value $|dB/dx|_{x_1}$ model, given in the lower right panel of Figure 5, is extremely flat. As $|dB/dx|_{x_1}$ is increased the field strength decreases across the domain in an almost linear fashion; for sufficiently large values the profile becomes nonlinear. Given that the change in density across a front is much more dramatic than that of the magnetic field strength, the ratio of the magnetic field strength to the number density of neutrals, B/n, changes markedly throughout the transition layer.

In Figure 6, we plot the plasma velocity profile, given by $v_p \approx v + v_D$ and Equation (6), of each of the front models of Figure 5. The shapes of the profiles are governed by the behavior of the magnetic field strength. The plasma velocity is almost constant across the lowest $|dB/dx|_{x_1}$ model since the magnetic field strength profile is close to flat, whereas the larger $|dB/dx|_{x_1}$ models show more variation in their plasma velocity profiles due to the presence of significant gradients in the magnetic field. In all cases, the drift velocity is positive and larger than the bulk velocity of the front, such that the plasma velocity is also positive.

In Figure 7, we compare the ion–neutral drift heating rate, given by Equation (16), to that of photoelectric heating, given by Equation (15), for each of the front models of Figure 5. The lowest $|dB/dx|_{x_1}$ model has a much smaller ambipolar drift heating rate than photoelectric heating rate which is why the structure of that front is barely different from the hydrodynamic case. The three larger $|dB/dx|_{x_1}$ fronts have larger ambipolar heating rates that are comparable to the photoelectric heating rate. These fronts depart more noticeably from the hydrodynamic solution and are less diffusive.

We also investigate the effect of magnetic field strength on front profiles at fixed initial $|dB/dx|_{x_1}$. Figure 8 shows a variety of front characteristics for initial field strengths of 1, 3, and 5 μG and $|dB/dx|_{x_1} = 308.6\ \mu\mathrm{G\ pc}^{-1}$. The temperature profiles are very similar, with the effect of increasing the field strength being larger temperature gradients at small scales and thinner fronts. The effect on the density profile is that the higher magnetic field

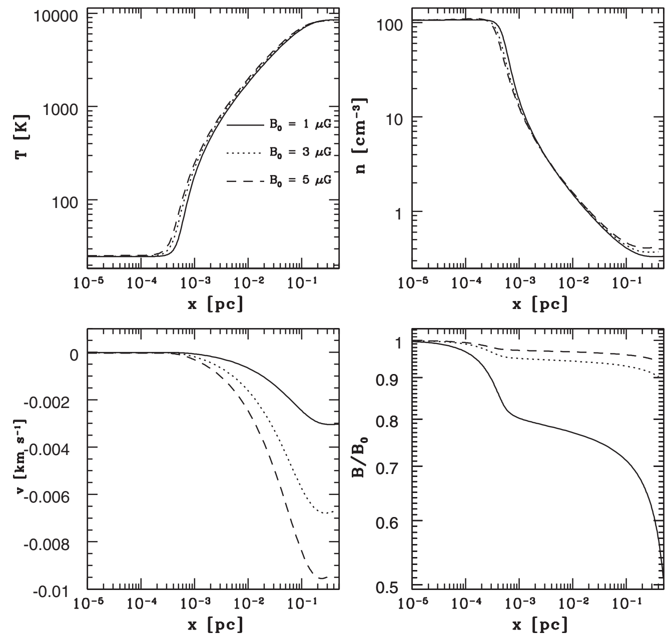

Figure 8. Temperature, density, bulk velocity, and magnetic field strength profiles of fronts having an initial density of $n = 106.08\ \mathrm{cm}^{-3}$ at various magnetic field strengths for fixed $|dB/dx|_{x_1} = 308.6\,\mu\mathrm{G\ pc}^{-1}$. The same line styles are also employed in Figures 9 and 10.

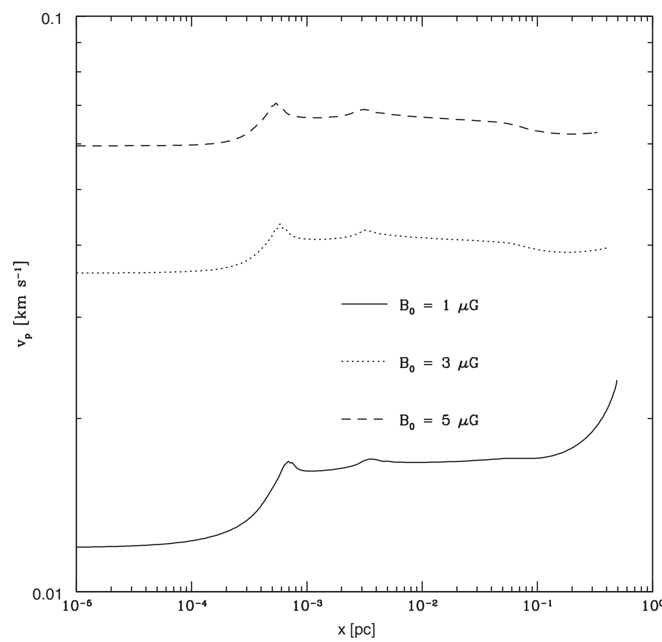

Figure 9. Plasma velocity profiles of fronts having an initial density of $n = 106.08\ \mathrm{cm}^{-3}$ at various magnetic field strengths for fixed $|dB/dx|_{x_1} = 308.6\,\mu\mathrm{G\ pc}^{-1}$.

strength fronts connect warm phases with higher densities. The velocity profiles are slightly negative, which implies that these are actually condensation fronts, and the departure from a static solution seems to increase with increasing field strength. Higher field strength solutions have flatter magnetic profiles because the efficiency of ambipolar diffusion increases with magnetic field strength.

In Figure 9, we plot the plasma velocity profiles of each of the front models of Figure 8. The size of the plasma velocity increases with increasing magnetic field strength and the shape of the profile becomes flatter. This is also due to the

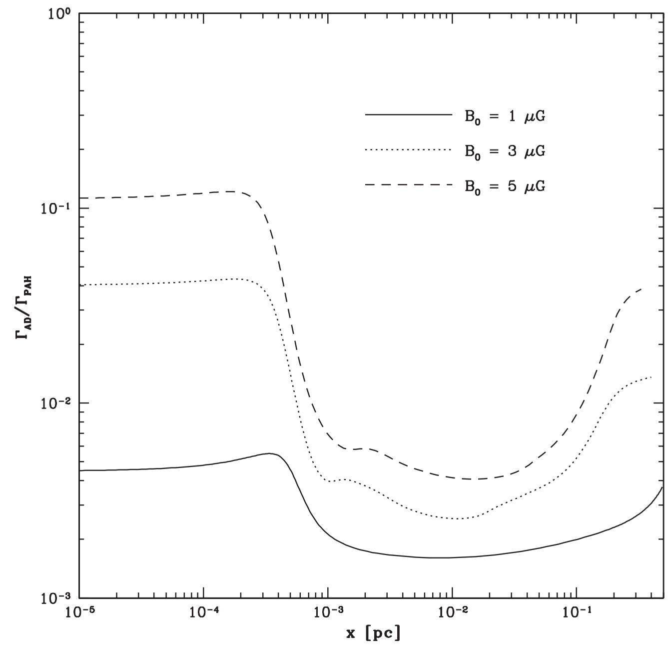

Figure 10. Ambipolar drift heating rates normalized by photoelectric heating rate across fronts having an initial density of $n = 106.08\ \mathrm{cm}^{-3}$ and various initial magnetic field strengths for fixed $|dB/dx|_{x_1} = 308.6\,\mu\mathrm{G\ pc}^{-1}$.

higher efficiency of ambipolar diffusion at larger magnetic field strengths.

In Figure 10, we compare the photoelectric and ambipolar heating rates for the front models shown in Figure 8. For these particular cases the photoelectric heating rate is larger than the ambipolar heating rate for all field strengths and the ambipolar heating rate increases with magnetic field strength.

4.3. *Flux-freezing Approximation*

For completeness, we also present the flux-freezing approximation, in which the behavior of the magnetic field is tied to the density such that B/ρ is constant in one dimension. This result can be obtained by computing the total derivative of the quantity B/ρ using the continuity and induction equations. To calculate the structure of a front in this approximation, we solve Equations (9) and (10) and everywhere replace B by $\rho\mathcal{C}$, where $\mathcal{C}$ is a constant. Including the definition $z \equiv dT/dx$, we have a system of three ODEs, which we solve using our shooting method, with the mass flux, j, the parameter to be adjusted. We impose the boundary conditions given by Equations (18) and (19), with no need for a condition on the magnetic field strength since its behavior is governed by that of the density.

Figure 11 shows solutions for an initial density of $n = 106.08\ \mathrm{cm}^{-3}$ at various initial magnetic field strengths. As the field strength is increased, the front becomes thinner and the transition reaches a progressively lower temperature, higher density final state at the right-hand boundary. Both the density and magnetic field strength span more than 2 orders of magnitude from one phase to the other. While such a range of densities is routinely observed in the neutral ISM, such widely varying magnetic field strengths are not (e.g., Troland & Heiles 1986) and this provides the first indication that the flux-freezing approximation is not suitable for our problem.

We go on to use these results to calculate ambipolar drift velocities, using Equation (6), and heating rates, given by Equation (16), throughout the front. These are plotted in the lower two panels of Figure 11. For the most extreme case shown,

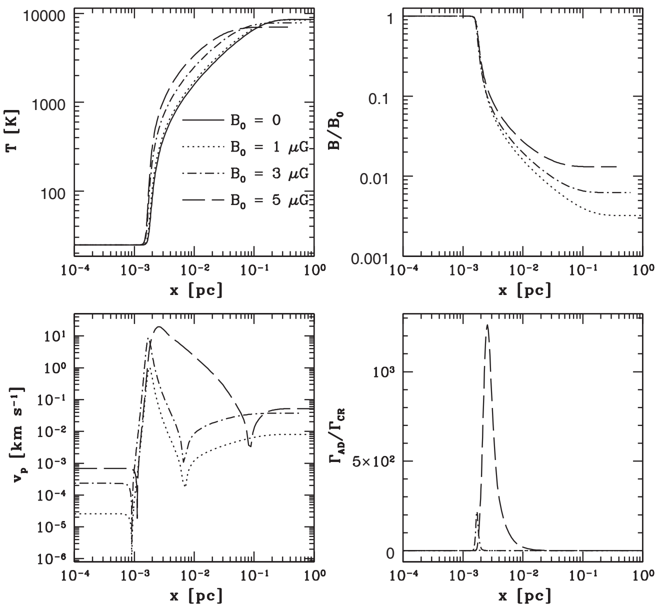

Figure 11. Profiles of fronts having an initial density of $n = 106.08$ cm^{-3}, hence, $p_{\rm thermal}/k_B = 2612$ K cm^{-3}, calculated in the flux-freezing approximation (without ambipolar drift heating) at various magnetic field strengths. The top panels show the temperature and magnetic field strength profiles. Although not shown here, the density profile has the same shape as the field strength profile, as dictated by flux freezing. The lower panels show the plasma velocity and the ratio of the ambipolar heating rate to the photoelectric heating rate. The solid line shows the hydrodynamic result, so it only appears in the upper left panel.

a saturated front with an initial density of 106.08 cm^{-3} and an initial magnetic field strength of 5 μG, we obtain a maximum drift velocity of 19.4 km s^{-1} and a maximum heating rate of 1.9×10^{-21} erg s^{-1} cm^{-3}, 3 orders of magnitude greater than the photoelectric heating rate. Although the equation for drift velocity breaks down for cases in which it is supersonic, we may still employ it to show that if the flux-freezing approximation held, the drift velocities and heating rates would be enormous. Such an outcome is not self-consistent with the rest of the model and allows us to argue that the solutions must be closer to what we have already presented, with the magnetic field strength almost constant over the extent of the front for cases in which ambipolar drift heating does not dominate. We thus suggest that by the time steady-state fronts are established in the neutral ISM the flux-freezing approximation does not apply.

5. DISCUSSION

We have shown the magnetic field strength profiles of fronts having ion–neutral drift heating rates much smaller than the photoelectric heating rate to be almost flat. In this section, we argue that it is the thin extent of these fronts that mediates the leakage of the magnetic field by ambipolar diffusion. We begin by using our results to justify our steady-state and ionization equilibrium assumptions. The minimum flow time through a front is of order $\tau_{\rm flow} \sim 0.01$ km s^{-1}/0.1 pc $\sim$ 10 Myr (refer to Figure 5). This should be compared to the ion–neutral collision time, given by $\tau_{\rm in} \sim (\rho_n \gamma_{\rm AD})^{-1} \sim 15.8/n_n$ yr. Thus, we have $\tau_{\rm in}/\tau_{\rm flow} \ll 1$, so are safe in our steady-state formulation of ambipolar diffusion. The assumption of ionization equilibrium is scrutinized by comparing $\tau_{\rm flow}$ to the recombination time for hydrogen, given by $\tau_{\rm rec} \sim 1/\alpha^{(2)} n$, where $\alpha^{(2)} \sim 2.06 \times 10^{-11}\, T^{-1/2}$ cm^3 s^{-1} (Spitzer 1978). For a front with an initial density of 106.08 cm^{-3}, we calculate a recombination time of $\sim$70 yr on the cold side and on the warm side we obtain $\sim$5000 yr. For all our other front models we also find $\tau_{\rm rec}/\tau_{\rm flow} \ll 1$, so for this work our simple single-fluid treatment of ambipolar diffusion will suffice.

We now present a diffusive description of fronts in which we compare the thermal and ambipolar diffusivities. Taking $U = nk_BT$ to be the energy density, we write the thermal timescale as $\tau_{\rm th} = U/\rho\mathcal{L}$ and the thermal diffusivity as $\lambda_{\rm th} = \kappa T/U$, such that the characteristic length scale of the problem, the Field length, is given by $l_F = \sqrt{\lambda_{\rm th}\tau_{\rm th}}$ (Field 1965; Begelman & McKee 1990). Hence, the thermal timescale and flow velocity may be written in terms of the thermal diffusivity, such that $\tau_{\rm th} \sim l_F^2/\lambda_{\rm th}$ and $v_{\rm th} \sim \lambda_{\rm th}/l_F$, respectively. In the magnetic field case, the field is redistributed diffusively, with ambipolar diffusivity, $\lambda_{\rm AD} = v_A^2 \tau_{\rm ni}$, where $\tau_{\rm ni}$ is the neutral–ion collision time, approximated by $\tau_{\rm ni} \sim 1.58 \times 10^3/n_i$ yr (Padoan et al. 2000). Comparing the thermal and ambipolar diffusivities we obtain

$$\frac{\lambda_{\rm th}}{\lambda_{\rm AD}} = \frac{\kappa}{nk_B v_A^2 \tau_{\rm ni}} \sim 10^{-2}\frac{n_i\, T^{1/2}}{B_\mu^2}, \tag{22}$$

where B_μ is the field strength in units of μG. We compute Equation (22) at both boundaries of our front models and for all cases we obtain $\tau_{\rm AD}/\tau_{\rm th} \ll 1$. For example, for a front with an initial density and magnetic field strength of 106.08 cm^{-3} and 5 μG, respectively, and $|dB/dx|_{x_1} = 308.6\ \mu$G pc^{-1}, we obtain $\tau_{\rm AD}/\tau_{\rm th} \sim 4.9 \times 10^{-5}$ on the cold side and $\tau_{\rm AD}/\tau_{\rm th} \sim 4.0 \times 10^{-4}$ on the warm side. This means the drift time is always much smaller than the time to flow through the front, suggesting that the field has time to become close to uniform.[4]

Our results show that increasing the ambipolar heating rate changes the structure of our front solutions. By balancing the ambipolar and photoelectric heating rates, Equations (15) and (16), and approximating the magnetic field strength gradient as $B_0/L_{\rm Bcrit}$, we can estimate the critical length scale at which the magnetic field becomes important in determining structure:

$$L_{\rm Bcrit} = \left(\frac{\lambda_{\rm AD} B_0^2}{4\pi n \Gamma_{\rm PAH}}\right)^{1/2}. \tag{23}$$

The magnetic length scale is given by $L_B \sim B/|\nabla B|$, so if $L_B > L_{\rm Bcrit}$ the effect of the field on the structure of a front is small. We compare L_B and $L_{\rm Bcrit}$ in Figure 12 for a front with an initial density of $n \sim 106.08$ cm^{-3} and initial field strengths of $B = 1$, 3, and 5 μG, with an initial field strength gradient of $|dB/dx|_{x_1} = 308.6\ \mu$G pc^{-1}. For the 5 μG case we obtain $L_B \sim 1.6 \times 10^{-2}$ pc and $L_{\rm Bcrit} \sim 5.4 \times 10^{-3}$ pc on the cold side, and on the warm side we find $L_B \sim 16.3$ pc and $L_{\rm Bcrit} \sim 2.9$ pc. The magnetic length scale is larger than the critical scale throughout the front; thus, ambipolar drift heating does not have a dramatic effect on the structure of a front.

Previous dynamical studies have claimed that ion–neutral drift is not a sufficiently fast diffusion process for transporting magnetic energy and instead invoked turbulent ambipolar drift (Heitsch et al. 2004) or turbulent magnetic reconnection (Santos-Lima et al. 2010) to explain the B–ρ relation. However, these studies were on larger scales than the fronts considered here. Our results suggest that for this simple scenario in which

[4] Note that the value of $|dB/dx|_{x_1}$ enters into this estimate only insofar as it affects the equilibrium temperature and front structure.

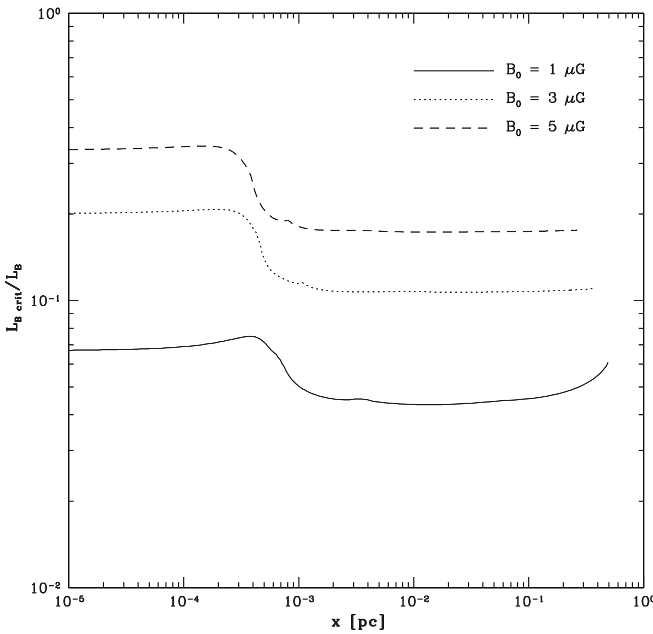

Figure 12. Ratio of the critical magnetic length scale to the magnetic length scale for fronts having an initial density of $n \sim 106.08$ cm^{-3} and various initial magnetic field strengths, with $|dB/dx|_{x_1} = 308.6\,\mu$G pc^{-1}. Ambipolar drift heating becomes important in determining the structure of the front if $L_B < L_{\rm Bcrit}$.

the phase transitions are thin, ambipolar diffusion alone is a sufficient mechanism for redistributing the magnetic field energy, without the need for turbulence. Our work directly complements a study of the thermal instability as a formation mechanism for diffuse H I clouds (Inoue et al. 2007). In that work, it was shown that ambipolar diffusion is a necessary and sufficient ingredient for the formation of a two-phase medium. Once that medium is established, the methods discussed in this paper may be applied to calculate its structure.

6. SUMMARY AND CONCLUSIONS

In this work, we have investigated the effect of magnetic fields on two-phase structure in the neutral ISM. We have presented a numerical method for calculating the one-dimensional structure of fronts separating the CNM from the WNM, including the effects of ambipolar diffusion. We showed that the pressure range over which two-phase structure is permitted becomes larger, by as much as a factor of 2, due to the contribution of ambipolar drift heating, with both the minimum and maximum pressures increasing from their hydrodynamic values. We find our magnetized front profiles to be very similar to the hydrodynamic solutions, and, in cases where photoelectric heating dominates ambipolar drift heating, to have close to flat magnetic field strength profiles. We also showed that the flux-freezing assumption yields unphysically large drift velocities and frictional heating rates. Our method is generic and, by including the appropriate physics, may be extended to other astrophysical multi-phase systems.

Although the one-dimensional picture discussed in this work is fairly simple, if the magnetic field strength and density were related we would have expected to see a correlation. Our results are consistent with the observational evidence that there is no relationship between magnetic field strength and density in interstellar atomic gas, which suggests that ambipolar diffusion is an efficient transport mechanism in the neutral ISM. The effect of ambipolar diffusion on the stability properties of thermal fronts will be the subject of forthcoming publications.

We acknowledge support from NASA ATP Grant NNGO5IGO9G and NSF Grant PHY0821899. Our work has benefited from useful discussions with J. E. Everett, F. Heitsch, K. M. Hess, A. S. Hill, N. A. Murphy, L. M. Nigra, and R. H. D. Townsend. We thank the referee for useful comments that enabled us to improve our manuscript.

REFERENCES

Begelman, M. C., & McKee, C. F. 1990, ApJ, 358, 375
Draine, B. T., Roberge, W. G., & Dalgarno, A. 1983, ApJ, 264, 485
Ferrière, K., Zweibel, E. G., & Shull, M. 1988, ApJ, 332, 984
Field, G. B. 1965, ApJ, 142, 531
Field, G. B., Goldsmith, D. W., & Habing, H. J. 1969, ApJ, 155, L149
Heiles, C., & Troland, T. H. 2005, ApJ, 624, 773
Heitsch, F., Zweibel, E. G., Slyz, A. D., & Devriendt, J. E. G. 2004, ApJ, 603, 165
Inoue, T., Inutsuka, S.-I., & Koyama, H. 2006, ApJ, 652, 1331 (IIK06)
Inoue, T., Inutsuka, S.-I., & Koyama, H. 2007, ApJ, 658, L99
Mestel, L. 1985, in Protostars and Planets II, ed. D. C. Black & M. S. Matthews (Tucson, AZ: Univ. Arizona Press), 320
Padoan, P., Zweibel, E. G., & Nordlund, A. 2000, ApJ, 540, 332
Parker, E. N. 1953, ApJ, 117, 431
Passot, T., & Vázquez-Semadeni, E. 2003, A&A, 398, 845
Penston, M. V., & Brown, F. E. 1970, MNRAS, 150, 373
Press, W. H., Teukolsky, S., Vetterling, W. T., & Flannery, B. P. 1992, Numerical Recipes in Fortran 77, The Art of Scientific Computing (2nd ed.; Cambridge: Cambridge Univ. Press)
Santos-Lima, R., Lazarian, A., De Gouveia Dal Pino, E. M., & Cho, J. 2010, ApJ, 714, 442
Scalo, J. H. 1977, ApJ, 213, 705
Shu, F. H. 1983, ApJ, 273, 202
Spitzer, L. 1978, Physical Processes in the Interstellar Medium (New York: Wiley)
Stone, J. M., & Zweibel, E. G. 2009, ApJ, 696, 233
Troland, T. H., & Heiles, C. 1986, ApJ, 301, 339
Wolfire, M. G., Hollenbach, D., McKee, C. F., Tielens, A. G. G. M., & Bakes, E. L. O. 1995, ApJ, 443, 152
Zel'dovich, Ya. B., & Pikel'ner, S. B. 1969, Sov. J. Exp. Theor. Phys., 29, 170
Zweibel, E. G. 2002, ApJ, 567, 962
Zweibel, E. G., & Brandenberg, A. 1997, ApJ, 478, 563